EBioMedicine 38 (2018) 79–88

Contents lists available at ScienceDirect

EBioMedicine

journal homepage: www.ebiomedicine.com

EBioMedicine
Published by THE LANCET

Research paper

Ectopic high endothelial venules in pancreatic ductal adenocarcinoma: A unique site for targeted delivery

Baharak Bahmani [a,1], Mayuko Uehara [a,1], Farideh Ordikhani [a], Xiaofei Li [a], Liwei Jiang [a], Naima Banouni [a], Takaharu Ichimura [b], Vivek Kasinath [a], Siawosh K. Eskandari [a], Nasim Annabi [c], Jonathan S. Bromberg [d], Leonard D. Shultz [e], Dale L. Greiner [f], Reza Abdi [a,*]

[a] Transplantation Research Center, Renal Division, Brigham and Women's Hospital, Harvard Medical School, Boston, MA 02115, USA
[b] Renal Division, Brigham and Women's Hospital, Harvard Medical School, Boston, MA 02115, USA
[c] Department of Chemical and Biomolecular Engineering, University of California Los Angeles, CA 90095, USA
[d] Department of Surgery and Microbiology and Immunobiology, University of Maryland School of Medicine, Baltimore, MD 21201, USA
[e] Department of Immunology, The Jackson Laboratory, Bar Harbor, ME 04609, USA
[f] Department of Molecular Medicine, University of Massachusetts Medical School, Worcester, MA 01605, USA

ARTICLE INFO

Article history:
Received 30 July 2018
Received in revised form 15 November 2018
Accepted 15 November 2018
Available online 27 November 2018

Keywords:
Pancreatic ductal adenocarcinoma
High endothelial venules
Peripheral node addressin
MECA79 coated nanoparticles
Taxol

ABSTRACT

Background: Nanomedicine offers an excellent opportunity to tackle treatment-refractory malignancies by enhancing the delivery of therapeutics to the tumor site. High endothelial venules (HEVs) are found primarily in lymph nodes or formed *de novo* in peripheral tissues during inflammatory responses. They express peripheral node addressin (PNAd), which is recognized by the monoclonal antibody MECA79.
Methods: Here, we demonstrated that HEVs form *de novo* in human pancreatic ductal adenocarcinoma (PDAC). We engineered MECA79 coated nanoparticles (MECA79-NPs) that recognize these ectopic HEVs in PDAC.
Findings: The trafficking of MECA79-NPs following intravenous delivery to human PDAC implanted in a humanized mouse model was more robust than non-conjugated NPs. Treatment with MECA79-Taxol-NPs augmented the delivery of Paclitaxel (Taxol) to the tumor site and significantly reduced the tumor size. This effect was associated with a higher apoptosis rate of PDAC cells and reduced vascularization within the tumor.
Interpretation: Targeting the HEVs of PDAC using MECA79-NPs could lay the ground for the localized delivery of a wide variety of drugs including chemotherapeutic agents.
Fund: National Institutes of Health (NIH) grants: T32-EB016652 (B·B.), NIH Cancer Core Grant CA034196 (L.D.S.), National Institute of Allergy and Infectious Diseases grants R01-AI126596 and R01-HL141815 (R.A.).

1. Introduction

Pancreatic ductal adenocarcinoma (PDAC) belongs to a lethal family of cancers [1,2], and it is estimated to become the second most common cause of cancer deaths by 2030 [3]. Although advanced surgical techniques, combinational chemotherapeutic agents, and adjuvant therapies have been employed to tackle this deadly disease, the overall prognosis of PDAC has remained unsatisfactory [4]. Nearly 80% of PDAC patients have an unresectable tumor at the time of diagnosis [2], and these patients experience a five-year survival of about 8% for all stages combined [5]. Among several obstacles that have plagued progress toward an effective therapy, an important factor hindering the penetration of chemotherapy drugs has been poor vascularization associated with the dense tumor tissue microenvironment [6–8]. One of the key features of PDAC is over-production of extracellular matrix fibers by pancreatic stellate cells, referred to as a desmoplastic reaction, which can result in a fibrotic and hypo-vascular environment that contributes to low drug penetration and delivery [9,10].

Nanotechnology provides opportunities to tackle treatment-refractory conditions, such as cancer, through smart systems of delivery for relevant drugs to the tumor sites. The majority of the earliest anticancer nanocarriers were designed on the basis of the enhanced permeability and retention (EPR) effect [11,12]. EPR delivery systems rely on the long-standing observation that tumor vasculature is leaky and thereby allows for high penetration of drugs within the tumor environment [13]. However, recent studies have questioned the role of EPR as a dominant mechanism that governs the trafficking of drugs to the site of the tumor [14]. For instance, the porosity of tumor vasculature has been found to be dependent on the individual tumor model. In addition, the

* Corresponding author at: Transplant Research Center, Brigham and Women's Hospital, 221 Longwood Ave, Boston, MA 02115, USA.
E-mail address: rabdi@rics.bwh.harvard.edu (R. Abdi).
[1] These authors contributed equally to this work.

https://doi.org/10.1016/j.ebiom.2018.11.030

Research in context

Evidence before this study

The high endothelial venule (HEV) is a highly specialized blood vessel found only in the lymph nodes (LN) and tonsils of healthy individuals. Assessment of the presence of HEVs in cancer tissues including PDAC has gained considerable interest recently. We have shown previously that MECA79 monoclonal antibody (mAb)-coated particles localize to the LN, where MECA79 mAb recognizes PNAd molecules expressed on the surface of the HEVs.

Added value of this study

Our data support the notion that the desmoplastic region of PDAC contains HEVs. Here, for the first time, we demonstrate that MECA79 mAb-coated particles home to implanted human PDAC in humanized mice. Treatment with MECA79-Taxol-NPs improved the efficacy of Paclitaxel significantly in suppressing the growth of PDAC.

Implications of all the available evidence

Our HEV-targeted platform of therapeutic delivery carries significant transformative potential in improving the treatment of PDAC, one of the most refractory human cancers.

uptake of nanoparticles (NPs) by Kupffer cells in the liver could reduce potentially the delivery of the drug to the tumor to a miniscule percentage (<1%) of the administered amount [15].

Active, targeted delivery often relies on surface modification of the NPs with an antibody or peptide to interact with a ligand or receptor of interest [16]. The interaction of NPs with an endothelial cell represents an early locus that can control the trafficking of circulating NPs to the targeted tissue. A limitation with this method of delivery is the ubiquitous expression of common molecules by endothelial cells, which may increase the rate of off-target effects [8].

The high endothelial venule (HEV) is a highly specialized blood vessel that is found only in the lymph nodes (LN) and tonsils in the usual healthy state [17]. In contrast to normal venules that contain flat endothelial cells, HEVs contain cuboid endothelial cells of greater height that express a series of sialyl-Lewis^X-coated proteins, referred to as peripheral node addressin (PNAd) molecules [17]. MECA79 is a monoclonal antibody (mAb) that recognizes all of the PNAd molecules [18]. Interestingly, HEVs are also formed ectopically in chronically inflamed tissues as well as in a wide variety of cancers including PDAC [19–22]. We have previously shown that microparticles coated with MECA79 localize to lymph nodes through their interaction with HEVs [23]. Given that MECA79 mAb also recognizes the ectopic HEVs in the tumors, we hypothesized that MECA79-coated NPs can home to PDAC by binding to the HEV structures in these tumors. Thus, MECA79-coated NPs afford opportunities to deliver chemotherapeutics to PDAC.

2. Materials and methods

2.1. Cell line, mice and human PDAC tissue

Human pancreatic adenocarcinoma cell line BxPC-3 (CRL-1687) was purchased from American Type Culture Collection (ATCC). NOD.Cg-*Prkdc*^{scid}*IL2rg*^{tm1Wjl}/SzJ (NSG) (JAX#005557) mice were obtained from The Jackson Laboratories. Male or female mice were used at 6–10 weeks of age and housed in sterilized, ventilated cages in a specific pathogen-free animal facility under a standard 12 h light/12 h dark cycle. Mice were fed irradiated food and water *ad libitum*. All animal experiments and methods were performed in accordance with the relevant guidelines and regulations approved by the Institutional Animal Care and Use Committee of Brigham and Women's Hospital, Harvard Medical School, Boston, MA. Human pancreatic ductal adenocarcinoma tumors for research purposes were collected at the University of Massachusetts Medical School under informed consent IRB ID: H00004721. The specimens were completely anonymous and had no direct identifiers and no codes or indirect identifiers that link back to subjects.

2.2. Synthesis of MECA79 conjugated NP

The poly(D,L-lactic-*co*-glycolic) acid (PLGA)-based copolymers were purchased from PolySciTech®, Akina Inc. Methoxy Poly (ethylene glycol)-b-PLGA copolymer (mPEG-PLGA, MW 5,000:30,000 Da, 50:50 LA:GA (w:w)) and PLGA-b-poly(ethylene glycol)-maleimide (PLGA-PEG-MAL, Mw ~30,000–5,000 Da, 50:50 LA:GA (w:w)) were used as the core polymers. The NPs were engineered using self-assembly single step nanoprecipitation. PEG-PLGA and maleimide-PEG-PLGA were dissolved in acetone. Paclitaxel (Taxol) (LC Laboratories, USA), Oregon Green™ 488 Conjugate (Oregon Green™ 488 labeled Taxol, Flutax-2, Thermo Fisher Scientific, US, referred to as *Taxol), or IRDye 800CW Carboxylate (LI-COR, USA) was added to the polymer mixture, vortexed and then added dropwise to a 0.015% aqueous solution of polyvinyl alcohol under vigorous stirring to formulate Taxol-NPs, *Taxol-NPs, or IR800-NPs. Then, the NP suspension was stirred for 2 h, and the NPs were concentrated by centrifugation using Amicon Ultra-15 centrifugal filter units (MWCO 100 kDa; Sigma-Aldrich) at 3,750 × rpm in intervals of 5 min. The resulting NPs were washed with Dulbecco's phosphate-buffered saline (DPBS) (Mediatech, Inc., Manassas, VA) and resuspended in 1 mL of DPBS.

The anti-mouse/human PNAd antibody (MECA79, NOVUS Biologicals) was conjugated to the functional group of NPs using thiol-maleimide chemistry. Tris(2-carboxyethyl)phosphine hydrochloride (TCEP, 0.5 M, Sigma-Aldrich) was used to cleave thiol groups of MECA79 mAb. 30 μg of MECA 79 mAb was mixed with 30 μl of TCEP and incubated for 15 min at room temperature, then it was mixed with the NP suspension. The MECA79-NPs were stored at 4 °C prior to use.

2.3. Characterization of NPs

The size distribution of NPs was determined using Dynamic Light Scattering (DLS) as previously described [24]. The morphology of NPs was observed by transmission electron microscopy (TEM). Freshly prepared NPs were deposited on 200-mesh Formvar/carbon-coated copper grids and negatively stained with 0.75% uranyl formate stain, before imaging with a Tecnai G2 Spirit BioTWIN electron microscope equipped with an AMT 2 k CCD camera and low-dose software. The loading of Taxol was determined using ultraviolet-visible (UV-VIS) spectrophotometer as previously described [24]. A calibration curve of the absorbance at 230 nm for various concentrations of Taxol was prepared. The absorbance of the supernatants and samples were compared with this calibration curve to determine the loading efficiency of Taxol.

2.4. Release kinetics of Taxol

To quantify the release profile of Taxol from the NPs, *Taxol-NPs or MECA79-*Taxol-NP were incubated at 37 °C in triplicate. At predetermined time intervals, the NPs were removed, transferred to Amicon Ultra-15 centrifugal filter units (MWCO 10 kDa; Sigma-Aldrich), and centrifuged at 3,750 × rpm for 5 min. The filtrate was analyzed with a UV-VIS spectrophotometer, and absorbance was measured at 488 nm to determine the amount of released Taxol at each time point.

2.5. MTT assay

The standard 3-(4,5-dimethylthiazol-2-yl)-2,5-diphenyl tetrazolium bromide (MTT) protocol was utilized to assay the cell viability. Briefly, the BxPC-3 cell line was cultured in a 96-well plate (2×10^5 cells/well) and incubated at 37 °C in 5% CO_2 overnight. Next, empty NPs, Taxol-NPs and free Taxol were added to the cells and incubated at 37 °C in 5% CO_2 for 24 h. Then, the MTT solution (5 mg/ml) was added to each well, and the cells were incubated for another 4 h. Upon removal of the MTT solution, the formed formazan crystals were solubilized with isopropanol for 15 min, and the proportion of formazan to the number of viable cells was determined by an absorbance microplate reader (Versa MAX, Molecular Devices).

2.6. Pancreatic tumor implantation

The human PDAC tumor was cut into 3–5 mm^3 pieces with a razor blade on a sterilized petri dish. A small incision was made in the skin on the lower back of NSG mice, and the PDAC tumor was implanted subcutaneously. The tumor growth was monitored three times per week by digital caliper (Fisherbrand™Traceable™Digital Calipers).

2.7. In vivo targeting of human PDAC by NPs

To study the trafficking of NPs, the tumor-bearing mice were anesthetized *via* inhalation of isoflurane/oxygen, and IR800-NPs or MECA79-IR800-NPs were administered intravenously. The trafficking of the fluorescently labeled NPs was studied using a UVP iBox® Explorer2™ Imaging Microscope equipped with a 750–780 nm excitation filter and an 800 nm long-pass emission filter. For live imaging, mice were anesthetized and placed inside the dark box in prone position. For *ex vivo* imaging, the mice were sacrificed *via* carbon dioxide inhalation and cervical dislocation. Then, the pancreatic tumors were harvested for imaging.

2.8. Immunofluorescence and Immunohistochemistry staining of tumor

Frozen OCT blocks of tumors were cut using a cryostat into 8-μm thick sections and were stained using anti-PNAd (MECA79), anti-human CD31 (WM59, BioLegend), anti-Caspase-3 (4-1-18, BioLegend), anti-Collagen I (abcam), anti-Collagen IV (abcam), anti-Fibronectin (abcam), anti-alpha smooth muscle Actin (α-SMA, abcam), HECA 452 (HECA-452, BioLegend), anti-human HLA-A,B,C antibody (W6/32, BioLegend) and anti-mouse/human Ki-67 (11F6, BioLegend) antibodies. DAPI (VECTASHIELD, Vector Laboratories Burlingame, CA) was used to stain the cell nuclei. The stained tissue sections were imaged using a fluorescent confocal microscope and an EVOS FL2 auto microscope. For immunohistochemistry (IHC) staining, the human post-mortem PDAC samples were stained with anti-mouse/human PNAd (MECA79).

2.9. PDAC treatment

When the size of the implanted tumor reached 8 mm in diameter, the mice were randomized into different groups and given specified treatments: Group #1 was the control and received no treatment; Group #2 received free Taxol; Group #3 received Taxol-NPs; and Group #4 received MECA79-Taxol-NPs. All mice received intravenous injections three times a week for two weeks, followed by twice a week for one week. The Taxol dose was fixed at 0.5 mg/kg among Groups #2–4. The body weight and tumor size of the animals were monitored throughout the treatment course.

Antitumor activity was evaluated in terms of tumor volume (V), in which l, w, and h are the length, width, and height of the tumor as measured by a digital caliper, defined as

$$V = l \times w \times h$$

The tumor growth inhibition (TGI), in which V_c and V_t are the volume of the control tumor and tumor in treated groups at the end of the study, respectively, and V_o is the average starting volume, was thus estimated as follows

$$TGI(\%) = \frac{(V_c - V_t)}{(V_c - V_o)} \times 100$$

2.10. RT-PCR assay

RNA was isolated with TRIZOL (Invitrogen), and the first strand of cDNA was synthesized using 1 μg of RNA and High-Capacity Reverse Transcriptase (Invitrogen). RT-PCR was performed with SYBR Green PCR reagents. RNA levels were normalized to the level of GAPDH and calculated as delta-delta threshold cycle (ΔΔCT). Primers used for RT-PCR are listed as follows: GAPDH-For: AGCCACATCGCTCAGACAC, GAPDH-Rev: GCCCAATACGACCAAATCC; VEGF-For: CTACCTCCACCATG CCAAGT, VEGF-Rev: GCAGTAGCTGCGCTGATAGA; All RT-PCR reactions were performed in triplicate.

2.11. Statistics

Two-way ANOVA or one-way ANOVA analysis were used for comparison of experimental groups. Student's *t*-test was used for comparison of two groups. Differences were considered to be significant for $^{*}p \le 0.05$, $^{**}p \le 0.01$ and $^{***}p \le 0.001$. Prism software was used for data analysis and to prepare graphs (GraphPad). Data represent mean ± SEM.

3. Results

3.1. Presence of ectopic HEVs in PDAC

As outlined above, HEVs are formed newly in some malignancies, including PDAC [25]. This characteristic provides an unprecedented opportunity to test the efficacy of HEV-targeted delivery for the treatment of PDAC. We screened six post-mortem PDAC samples. All of these tissues contained *de novo* HEVs, when analyzed by immunohistochemistry staining of PNAd (marked with asterisks in Fig. 1a, 1–6). The cuboid endothelial cells of the HEV can be observed in a high-magnification IHC image of a $PNAd^+$ vessel in the PDAC tumor (Fig. 1b).

We propagated PDAC tumor samples (using NSG mice) from a tumor that was resected from a patient with advanced PDAC. Implants were placed in NSG mice, and the tumor was removed to assess the presence of HEV post-implantation. Immunohistochemistry showed the presence of *de novo* HEVs (ectopic HEVs) in this PDAC sample (Fig. 1c). Further localization of the PDAC *via* immunofluorescence staining showed the presence of HEVs within the dense desmoplastic regions of the tumor (Fig. 1d). The HEV structures were detected within the dense extracellular matrix (ECM) of the PDAC, as evidenced by staining the ECM components with fibronectin and α-smooth muscle actin (α-SMA), as shown in Fig. 1d [26]. To prove further that these vascular structures were HEVs, we also used HECA452 antibody (recognizes sialyl $Lewis^x$), which stained the structures that were identified as HEVs (Supplementary Fig. 1a). The use of human Class I HLA antibody revealed that the HEVs co-stained with anti PNAD antibody, suggesting that at least a portion of these HEVs remain of human origin (Supplementary Fig. 1b).

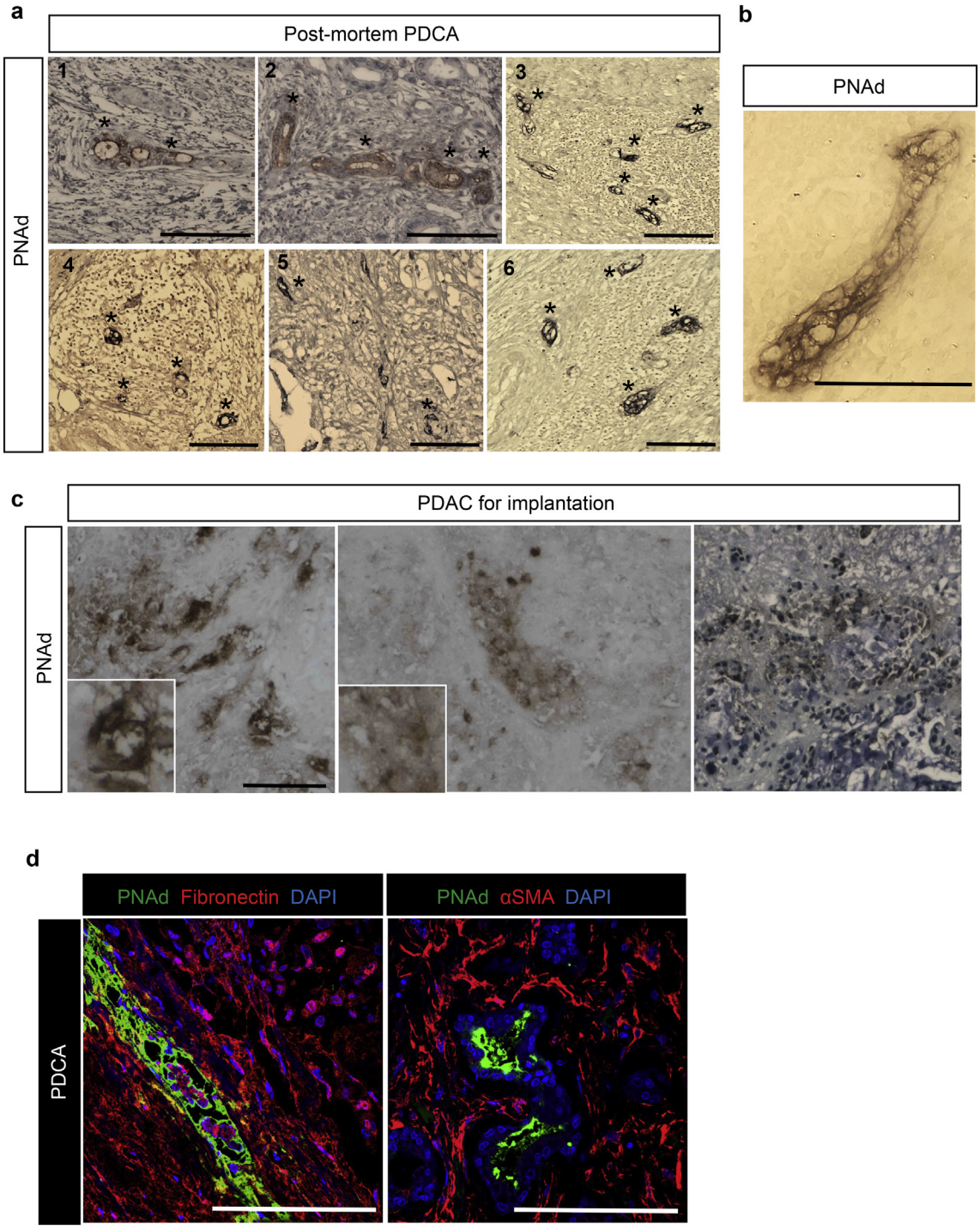

Fig. 1. Immunohistochemistry and immunofluorescence analysis of human PDAC. (**a**) Representative images from immunohistochemistry analysis of human PDAC samples from post-mortem showing ectopic PNAd$^+$ venules (marked by * in the images, $n = 6$, scale bar = 100 μm). (**b**) A representative high-magnification IHC image of a PNAD$^+$ vessel in the PDAC (Scale bar = 75 μm). (**c**) Immunohistochemistry staining of the human PDAC prior to implantation into the NSG mice confirming PNAd expression in the tissue. (**d**) Representative images of PNAD$^+$ vessels (green) surrounded by Fibronectin (red) and αSMA (red) (Scale bar = 100 μm).

3.2. Targeting PDAC in NSG mice using MECA79-IR800-NPs

Next, we tested the capacity of MECA79-NPs to localize to human PDAC following implantation into NSG mice. The PDAC-bearing NSG mice were injected with MECA79-IR800-NPs or non-conjugated IR800-NPs intravenously and imaged after 24 h. MECA79-IR800-NPs trafficked to the PDAC at a greater rate than that of the untreated control and non-conjugated IR800-NPs ($n = 4$ mice/group) (Fig. 2a). The mean fluorescence intensity (MFI) of the PDAC in the MECA79-NP-injected mice was significantly higher than the mice injected with non-conjugated IR800-NPs ($4.5 \pm 0.5 \times 10^4$ *vs.* $1.1 \pm 0.2 \times 10^4$, $^{***}p < 0.001$, student's *t*-test, n = 4 mice/group) (Fig. 2b). We also examined PDAC tissue to assess the pattern of trafficking of MECA79-IR800-NPs. The MECA79-IR800-NPs (in red) were localized

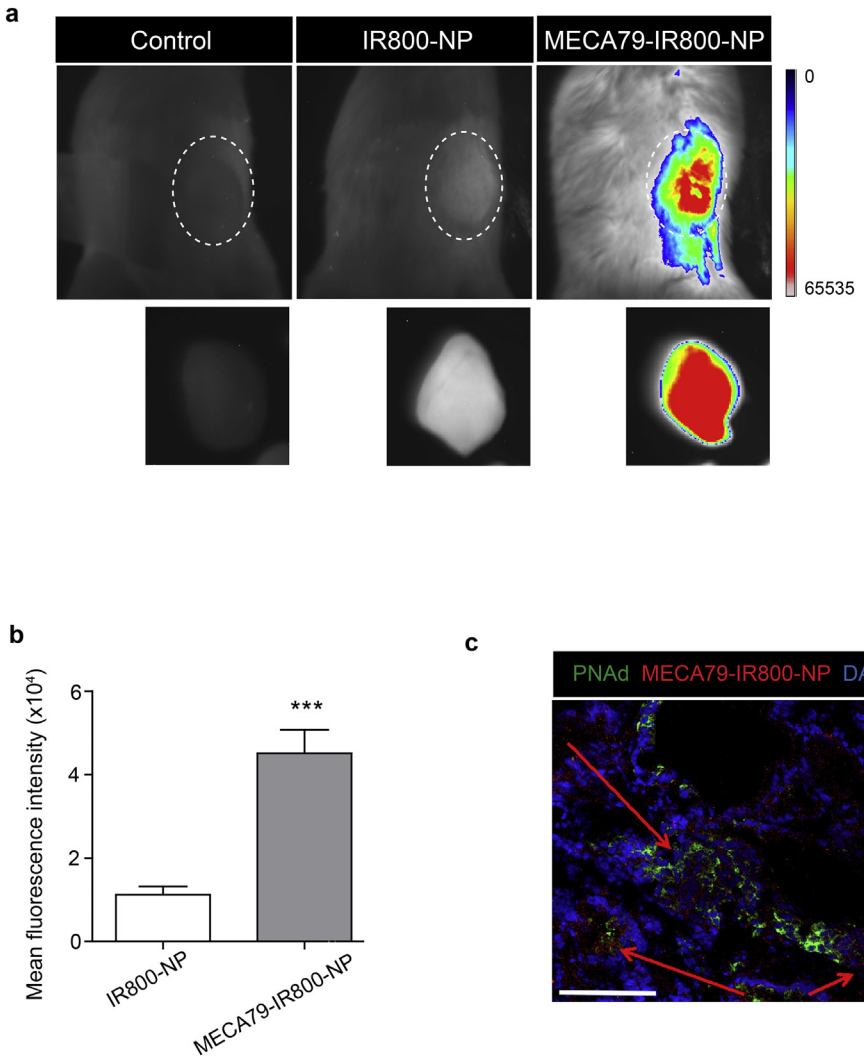

Fig. 2. Targeted delivery of NP to the PNAd-expressing HEV in PDAC. (**a**) Whole-body NIR fluorescent imaging showing higher trafficking of MECA79-IR800-NPs to PDAC, as compared to non-conjugated IR800-NPs. The dashed area in each image represents the PDAC tumor *in vivo* and *ex vivo* post-harvest, respectively. (**b**) Corresponding MFI of the tumor showing a significant increase in trafficking of MECA79-IR800-NPs, as compared to the non-conjugated IR800-NPs. The data are presented as the mean and SEM (n = 3). (***$p < 0.001$, student's *t*-test). (**c**) Representative immunofluorescence micrograph of the tumor 24 h post-injection of MECA79-IR800-NPs (red) demonstrates their presence around HEV (green). The red arrows point to the areas of MECA79-IR800-NP accumulation in the tumor (Scale bar = 100 μm).

to the vicinity of HEVs (in green) in the tumor (Fig. 2c). The arrows point to the areas of accumulation of MECA79-IR800-NPs in the tumor section.

3.3. Synthesis and characterization of MECA79-Taxol-NPs

We evaluated whether our model of targeted trafficking of NPs results in increased delivery and improved efficacy of a chemotherapeutic drug. We synthesized PLGA-based NPs encapsulating paclitaxel (Taxol-NPs). Fig. 3a shows the electron microscopy imaging of Taxol-NPs with spherical shape. The surface of the NPs was then modified with MECA79 mAb to form a delivery platform to target HEVs within PDAC. The average size of MECA79-Taxol-NPs was significantly higher than the Taxol-NPs (123.7 ± 8.2 nm *vs.* 80.9 ± 2.8, **$p < 0.01$, student's *t*-test, $n = 5$/group) (Fig. 3b). The Taxol was released from the NPs in a sustained manner during a one-week time period (Fig. 3c). The loading efficacy of Taxol in the NPs varied between 15%–30%.

Next, we tested the efficacy of Taxol-NPs in killing pancreatic adenocarcinoma cells *in vitro* using the MTT assay. The Taxol-NPs were as effective as free Taxol and resulted in significant tumor cell death (Fig. 3d).

Oregon Green™ 488 Taxol (*Taxol) was used to confirm the targeted delivery of Taxol to tumor. Either *Taxol or MECA79-*Taxol-NP was injected intravenously into PDAC-bearing NSG mice, and tumors were harvested 24 h post-injection for *ex vivo* imaging. The MFI of tumors was significantly higher in the MECA79-*Taxol-NP group, as compared to the *Taxol group (Fig. 3e). Immunofluorescence imaging of the PDAC tissue showed that more MECA79-*Taxol-NPs were present within the ECM of the tumor, as compared to the control group (Fig. 3f).

3.4. Therapeutic efficacy of MECA79-Taxol-NPs

We investigated the efficacy of MECA79-Taxol-NPs in the treatment of PDAC in NSG mice. Tumors were implanted into NSG mice, and the mice were randomized on the basis of tumor size and assigned to four different groups: control (no treatment), free Taxol, Taxol-NPs, and MECA79-Taxol-NPs.

The results demonstrated a marked reduction in the size of the PDAC during the course of treatment. The size of the tumor at the end of the study was significantly lower in mice treated with MECA79-Taxol-NPs ($1.4 \pm 0.4 \times 10^3$ mm^3), as compared to the no treatment group (6

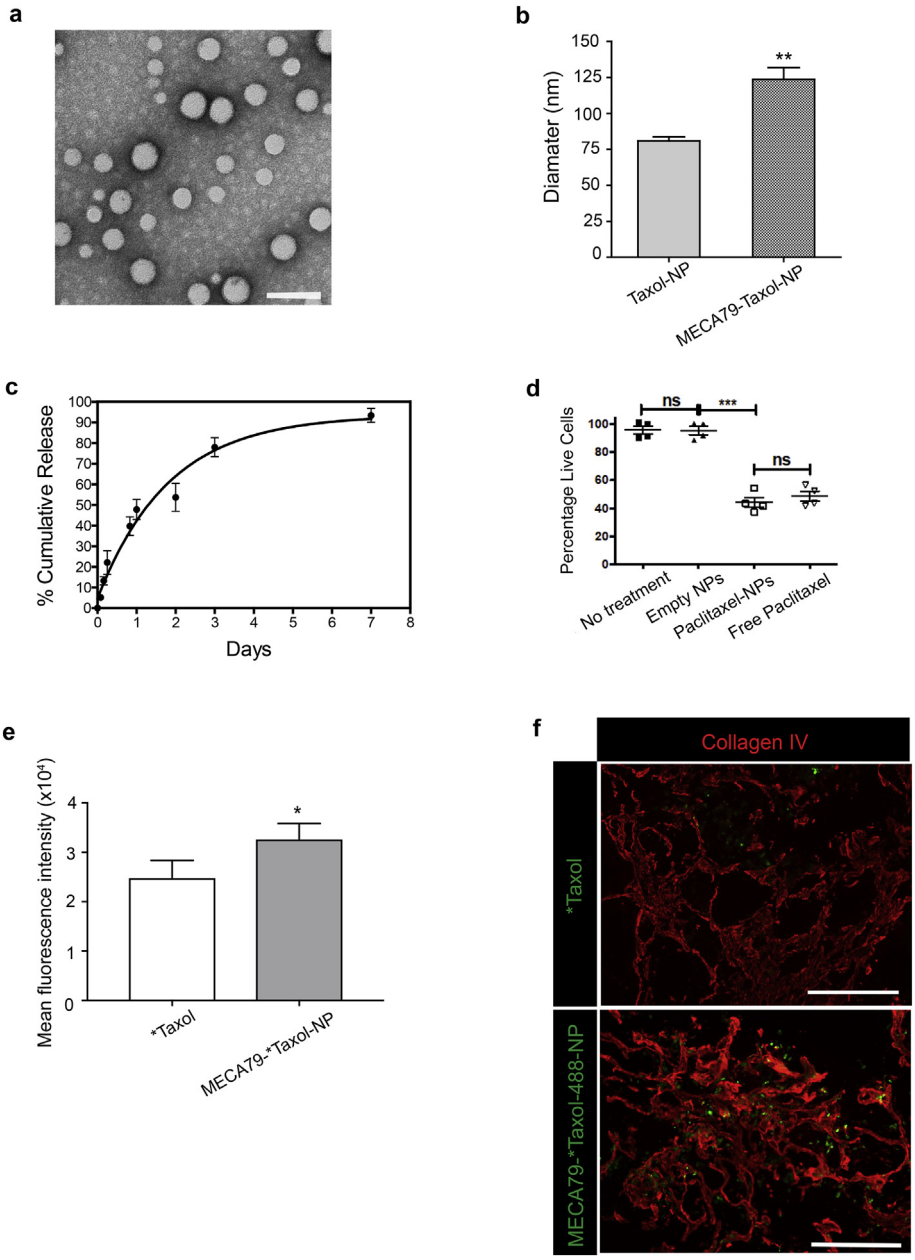

Fig. 3. Formulation and characterization of MECA79-Taxol-NPs. (**a**) Representative TEM images of Taxol-NP (Scale bar = 100 nm) (**b**) Hydrodynamic diameter of non-conjugated and MECA79-conjugated Taxol-NPs. The data are presented as the mean and SEM (n = 6). (**c**) Release kinetics of Taxol from NPs over one-week. The data are presented as the mean and SEM (n = 3). (**d**) Taxol-NPs induced similar levels of apoptosis in pancreatic cancer cells *in vitro* in comparison to free Taxol. (**e**) The MFI of tumors showed significantly higher accumulation of *Taxol in MECA79-*Taxol-NP group, as compared to *Taxol group (*$p < 0.05$, student's *t*-test). The data are presented as the mean and SEM (n = 3). (**f**) Immunofluorescence staining of PDAC tissue showed that MECA79-*Taxol-NPs (green) were present within the ECM (Collagen IV, in red) of tumor at a higher number, as compared to the control group (Scale bar = 100 μm).

$\pm$ 1.4 $\times$ 10^3 mm^3), the free Taxol treatment group (3.3 $\pm$ 0.3 $\times$ 10^3 mm^3), or the Taxol-NP treatment group (4.2 $\pm$ 1.3 $\times$ 10^3 mm^3, ***$p < 0.001$, ANOVA, $n = 5$ mice/group) (Fig. 4a). Non-conjugated Taxol-NP treatment, which relies solely on the EPR effect, was not effective, and the average size of the tumor in this group was similar to no treatment and free Taxol treatment groups. Furthermore, the final weight of the tumors in the mice treated with MECA79-Taxol-NPs was significantly smaller in comparison to the no treatment, free Taxol, and Taxol-NP treatment groups (Taxol dose = 0.5 mg/kg, *$p < 0.05$, **$p < 0.01$, ANOVA, n = 5 mice/group) (Fig. 4b). Representative images of tumors from each group at the end of the study are shown in Fig. 4b.

Finally, we calculated the tumor growth inhibition rate for each treatment group. The tumor growth inhibition rate almost doubled when mice were treated with MECA79-Taxol-NPs, as compared to the mice treated with a similar dose of free Taxol (68.02 $\pm$ 1.8 *vs.*36.91 $\pm$ 0.5, ***$p < 0.001$, student's *t*-test, n = 5 mice/group).

3.5. Immunofluorescence characterization of the PDAC

Assessment of the tumor tissue by immunofluorescence staining post-treatment revealed the presence of more apoptotic cells (caspase-3^+, Fig. 5a) in the targeted treatment group in comparison to the other groups. Caspase-3 is one of the cysteine proteases associated with Taxol-induced programmed cell death [27]. The percentage of caspase-3^+ cells doubled when the mice were treated with MECA79-Taxol-NPs (66.42 $\pm$ 2.84%), as compared to Taxol-NPs

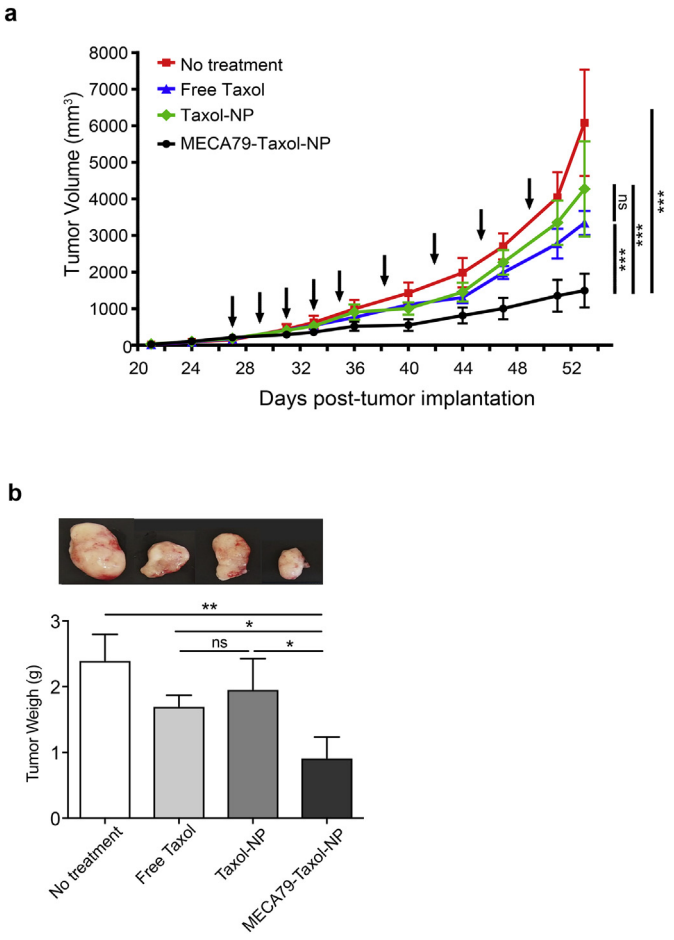

Fig. 4. Therapeutic efficacy of MECA79-Taxol-NPs. (**a**) Improved efficacy in delivering Taxol to PDAC was observed in mice treated with MECA79-Taxol-NPs, as compared to no treatment, free Taxol, and Taxol-NPs (Taxol dose =0.5 mg/kg, $^{***}p < 0.001$, ANOVA, n = 5 mice/group). Arrows indicate the days of treatment. The data are presented as the mean and SEM. (**b**) The final weight of the tumor in mice treated with MECA79-Taxol-NPs was significantly lower, as compared to the no treatment, free Taxol, and Taxol-NP treatment groups. ($^{*}p < 0.05$, $^{**}p < 0.01$, ANOVA, n = 5 mice/group). The data are presented as the mean and SEM.

(29.25 ± 2.17%) and free Taxol (36.58 ± 2.74%) (Fig. 5b). Apoptotic cells were located in close proximity to the vasculature ($CD31^+$ and HEV, Fig. 5c). In addition, immunofluorescence staining of the PDAC using a cellular marker of proliferation (Ki67) demonstrated a higher percentage of $Ki67^+$ cells in the Taxol-NP group, as compared to the MECA79-Taxol-NP group (47.7 ± 2.9% *vs.* 14.4 ± 1.8%, $^{***}p < 0.0001$, student's *t*-test) (Fig. 5a and d). Proliferating cells were located around the $CD31^+$ vasculature, but we observed very few around the HEV (Fig. 5e).

The PDAC in mice treated with MECA79-Taxol-NPs also demonstrated lower vascularization (CD31) as compared to the other groups (Fig. 5a). To assess the activity of vascular cells, the expression levels of VEGF genes were compared between the four groups. The expression of VEGF downregulated significantly in the tumor following treatment with MECA79-Taxol-NPs, while the expression levels remained the same in the no treatment, free Taxol, and Taxol-NP treatment groups (Supplementary Fig. 2a). Diminished microvessel intensity and VEGF expression levels have been reported previously as a result of Taxol treatment [28]. Taken together, our findings that demonstrate higher cellular apoptosis, along with lower cellular proliferation and vascularization, demonstrate efficient delivery of Taxol to PDAC using our targeted platform. To evaluate the changes in ECM deposition, PDAC tumors from the control and MECA79-Taxol-NP treatment groups were stained for Collagen I. Interestingly, Collagen I deposition was decreased, and the matrix became thinner and disrupted in the MECA79-Taxol-NP treated mice as compared to the control group (Fig. 5f).

4. Discussion

PDAC remains one of the most lethal malignancies [1,2]. Nearly 80% of PDAC patients are not eligible for tumor resection at the time of diagnosis, due to the presence of locally advanced disease or distant metastases. The mainstay of treatment for patients with advanced PDAC is palliative therapies, including chemotherapy and radiation [29]. Gemcitabine-based combination therapy has gathered momentum recently, but the overall prognosis for PDAC remains dismal [30,31]. Therefore, the development of an innovative therapeutic strategy aimed at improving the outcomes of PDAC patients constitutes a major unmet need.

The use of NPs provides an opportunity to target various pathological arms of PDAC. NPs can be modified for a number of variables to improve their anti-tumor efficacy, including charge, size, and shape [32,33]. A few reports have described the use of NPs to counter resistance toward gemcitabine. One method utilizes NPs to improve the overall kinetics of gemcitabine (*i.e.*, increasing its half-life) or to increase the cellular uptake of gemcitabine by the tumor [34]. Others have formulated polymeric NPs encapsulating curcumin, which increased its systemic bioavailability and resulted in increased suppression of PDAC in animals, as compared to free drugs [35]. The utility of NPs also centers on their potential to target specific molecular targets of the cancer. Epidermal growth factor receptor (EGFR) [36–39], Mucin 1 (MUC1) [40], and Plectin-1 [41] are among the receptors on the surface of cancer cells being used to target PDAC. These tumor cells are not in direct continuity with the blood.

The dense microenvironment of the PDAC is a key feature of PDAC that contributes to its resistance to therapeutic agents [42]. The dense stroma of PDAC (a result mainly of overproduction of ECM by stromal cells) is largely hypovascular, which restrains the penetrance of therapeutics [43]. The dense microenvironment of PDAC contributes to its immune evasion as well. Therefore, a significant interest has arisen to modulate the PDAC stroma in order to increase the efficacy of therapeutics [7,44–46], such as various transgenic mouse models in which genetically, enzymatically or pharmacologically induced remodeling of the stroma can increase the penetrance of gemcitabine.

One obstacle facing most treatment strategies is poor delivery of the drugs to the site of the tumor. Albumin-bound paclitaxel particles (nab-Paclitaxel) that interact with endogenous albumin transporters on endothelial cells of the tumor have been shown to traverse these cells effectively [47]. Liu et al. have targeted neuropilin-1 (NRP-1) on PDAC tumor vasculature in order to increase the penetration of silica NPs into the tumor [48]. They tested the co-administration of silica NPs and the cyclic tumor-penetrating peptide iRGD in patient-derived PDAC xenografts with low and high NRP-1 expression levels. They found that the silica NPs accumulated more extensively in the tumor with elevated levels of NRP-1 expression.

Our delivery platform has several unique qualities. PNAd-expressing HEVs are found in LNs normally, but PDAC peculiarly forms *de novo* HEVs [25]. Similarly, others have also demonstrated the expression of HEVs by other types of cancer and their potential implications in lymph node metastasis [49]. Our histological data indicate that these HEVs are embedded within the dense stroma. Targeting HEVs here presents an invaluable opportunity to develop a platform that could deliver several antineoplastic molecules that modulate the stromal milieu or enhance the local anti-tumor immune response. As noted in our histology data, chemotherapeutic agents could also target fibroblasts that surround the HEV, as demonstrated by their high expression of caspase-3.

Our delivery method can also target metastatic lesions hidden in the LNs. We have demonstrated previously that MECA79-coated particles can localize to HEVs in lymph nodes [24,50]. We were unable to address

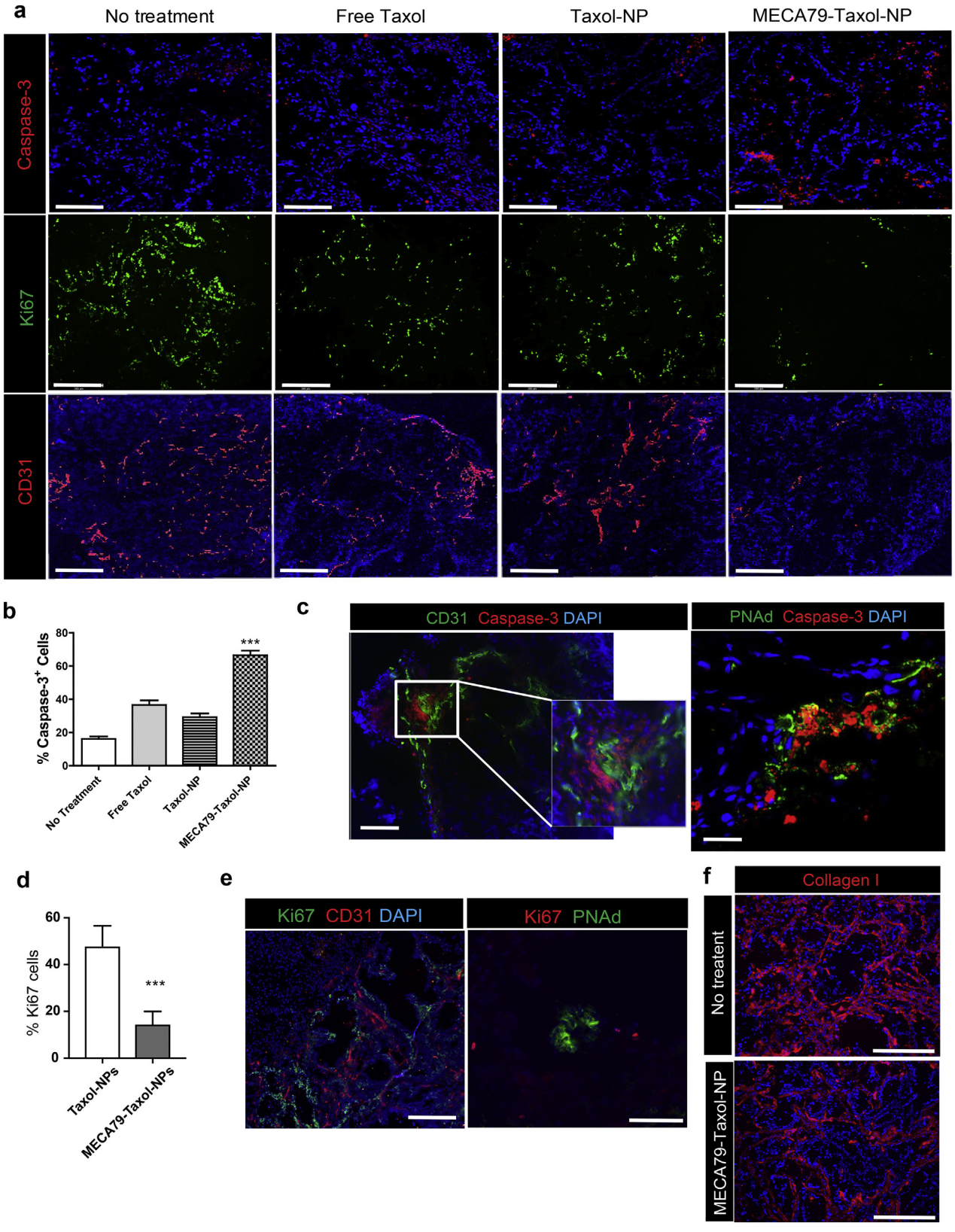

Fig. 5. Histological analysis of PDAC following treatment with MECA79-Taxol-NPs. (**a**) Immunofluorescence staining of the tumor at the end of the study demonstrated that treatment with MECA79-Taxol-NPs resulted in higher apoptosis (caspase-3^+) of cancer cells, lower cellular proliferation ($Ki67^+$), and decreased vascularization ($CD31^+$) (Scale bar = 200 μm). (**b**) Quantification of the caspase-3^+ cells using ImageJ software (***$p < 0.001$, ANOVA, n = 3 mice/group). The data are presented as the mean and SEM. (**c**) Representative immunofluorescence images of the PDAC tumor for markers of vasculature (CD31 and PNAd in green) and apoptosis (caspase-3 in red) following treatment with MECA79-Taxol-NPs (Scale bar = 200 μm). (**d**) Quantification of the $Ki67^+$ cells using ImageJ software (***$p < 0.001$, student's *t*-test, n = 3 mice/group). The data are presented as the mean and SEM. (**e**) Representative immunofluorescence images of the PDAC tumor for markers of vasculature (CD31 and PNAd) and proliferation (Ki67) in the no-treatment group (Scale bar = 200 μm for CD31, 100 μm for PNAd). (**f**) Immunofluorescence staining for collagen I (red) of the PDAC tumor comparing the groups that received no treatment and MECA79-Taxol-NP (Scale bar = 100 μm).

involvement of the LNs by PDAC in our mouse model (as NSG mice lack LNs), but the efficacy of our strategy to target metastatic niches in LNs should be explored in the future, as PDAC commonly metastasizes to local and distant LNs [51]. Many PDAC patients die with advanced metastasis to the liver and lungs [52]. Metastatic lesions in lungs and liver may also form *de novo* HEVs. Future specific metastatic animal models are required to examine the presence of HEVs in metastatic lesions, especially in the liver and lungs.

The treatment of complex medical conditions often requires combinatorial strategies that target various pathologic arms of the disease. Though we used a standard chemotherapy drug to demonstrate a proof of concept in this study, future studies can focus on delivering more specific modulators. One example is to deliver agents that dampen the activity of regulatory T cells but potentiate the activity of effector immune cells [53]. The other important feature is that our NPs target endothelial cells primarily, rather than relying on passive accumulation. Interestingly, HEVs were found within the dense stroma of the pancreas. Our delivery platform could provide opportunities to deliver modulators of the extracellular matrix (ECM) to PDAC as well. Finally, the potential significance of our HEV-targeted delivery platform lies in its capacity to provide molecular imaging to detect the early formation of malignant tumors and LN metastasis. Expansion of HEVs is one of the earliest changes that occurs in LNs following invasion by cancer, a phenomenon that can be traced by devising tagged MECA79-NPs [17]. Furthermore, *de novo* formation of HEV in the pancreas can be detected with high positive predictive value, given that a normal pancreas does not contain HEVs. Indeed, the development of a molecular imaging technique that will enhance the ability to properly diagnose and stage PDAC in its nascent phase is a major unmet need that could improve its overall outcome.

Several limitations can be addressed in the future to further advance our delivery platform. Here, we used Taxol, but one could envision better efficacy with somewhat more promising drugs, such as gemcitabine or devising a combinatorial strategy with a newer agent such as oteracil [54]. Assessment of the efficacy of our delivery platform in treating metastatic niches in peripheral organs would also be a valuable pursuit, as these niches also may express HEV. Such an investigation would require the development of a predictable mouse model with metastatic PDAC lesions. Lastly, a more comprehensive examination of the pattern of HEV formation within the tumor, in regard to its vicinity with actual tumor or vasculature, its development, and its progression can greatly help to better predict and/or develop effective therapeutic strategies. Finally, testing the efficacy of our delivery platform in other types of HEV-bearing malignancies would add greater rigor.

Of note, emerging data indicate the presence of HEVs in other malignancies, such as metastatic melanoma, adenocarcinoma of the colon, breast cancer, and non-small cell lung cancer [55,56]. Therefore, our new delivery platform can provide an avenue for the development of the next generation of nano-targeted modalities for the treatment of lethal cancers.

Author contributions

B.B designed and fabricated NP, designed and performed experiments, analyzed data and wrote the manuscript. M.U. designed and performed experiments, microsurgery, analyzed data, and wrote the manuscript. F.O., X. L., L.J., N.B., T.I., V.K. and S.K.E performed experiments. N.A., J.S.B., L.D.S., and D.L.G helped with study design and critically revised the manuscript. R.A. designed the study, interpreted and analyzed data, and critically revised and finalized the manuscript.

Declaration of interests

The authors have declared that no conflict of interest exists.

Acknowledgments

This work is in part supported by the following National Institutes of Health (NIH) grants: T32-EB016652 (B.B.), NIH Cancer Core Grant CA034194 (L.D.S.), National Institute of Allergy and Infectious Diseases grants R01-AI126596 and R01-HL141815 (R.A.).

Appendix A. Supplementary data

Supplementary data to this article can be found online at https://doi.org/10.1016/j.ebiom.2018.11.030.

References

[1] Siegel RL, Miller KD, Jemal A. Cancer statistics, 2016. CA Cancer J Clin 2016;66(1):7–30.
[2] Kleeff J, Korc M, Apte M, La Vecchia C, Johnson CD, Biankin AV, et al. Pancreatic cancer. Nat Rev Dis Prim 2016;2:16022.
[3] Ying H, Dey P, Yao W, Kimmelman AC, Draetta GF, Maitra A, et al. Genetics and biology of pancreatic ductal adenocarcinoma. Genes Dev 2016;30(4):355–85.
[4] Ryan DP, Hong TS, Bardeesy N. Pancreatic Adenocarcinoma. N Engl J Med 2014;371(11):1039–49.
[5] Chiaravalli M, Reni M, O'Reilly EM. Pancreatic ductal adenocarcinoma: State-of-the-art 2017 and new therapeutic strategies. Cancer Treat Rev 2017;60:32–43.
[6] Long J, Zhang Y, Yu X, Yang J, Lebrun D, Chen C, et al. Overcoming drug resistance in pancreatic cancer. Expert Opin Ther Targets 2011;15(7):817–28.
[7] Neesse A, Algul H, Tuveson DA, Gress TM. Stromal biology and therapy in pancreatic cancer: a changing paradigm. Gut 2015;64(9):1476–84.
[8] Minchinton AI, Tannock IF. Drug penetration in solid tumours. Nat Rev Cancer 2006;6(8):583–92.
[9] Dimou A, Syrigos KN, Saif MW. Overcoming the stromal barrier: technologies to optimize drug delivery in pancreatic cancer. Ther Adv Med Oncol 2012;4(5):271–9.
[10] Longo V, Brunetti O, Gnoni A, Cascinu S, Gasparini G, Lorusso V, et al. Angiogenesis in pancreatic ductal adenocarcinoma: a controversial issue. Oncotarget 2016;7(36):58649–58.
[11] Danhier F, Feron O, Preat V. To exploit the tumor microenvironment: passive and active tumor targeting of nanocarriers for anti-cancer drug delivery. J Control Release 2010;148(2):135–46.
[12] Din FU, Aman W, Ullah I, Qureshi OS, Mustapha O, Shafique S, et al. Effective use of nanocarriers as drug delivery systems for the treatment of selected tumors. Int J Nanomedicine 2017;12:7291–309.
[13] Nichols JW, Bae YH. EPR: evidence and fallacy. J Control Release 2014;190:451–64.
[14] Sykes EA, Chen J, Zheng G, Chan WC. Investigating the impact of nanoparticle size on active and passive tumor targeting efficiency. ACS Nano 2014;8(6):5696–706.
[15] Tavares AJ, Poon W, Zhang YN, Dai Q, Besla R, Ding D, et al. Effect of removing Kupffer cells on nanoparticle tumor delivery. Proc Natl Acad Sci U S A 2017;114(51) E10871-e80.
[16] Bazak R, Houri M, Achy SE, Kamel S, Refaat T. Cancer active targeting by nanoparticles: a comprehensive review of literature. J Cancer Res Clin Oncol 2015;141(5):769–84.
[17] Bahmani B, Vohra I, Kamaly N, Abdi R. Active targeted delivery of immune therapeutics to lymph nodes. Curr Opin Organ Transplant 2017;23:8–14.
[18] Hemmerich S, Butcher EC, Rosen SD. Sulfation-dependent recognition of high endothelial venules (HEV)- ligands by L-selectin and MECA 79, and adhesion-blocking monoclonal antibody. J Exp Med 1994;180(6):2219–26.
[19] Hiraoka N, Ino Y, Yamazaki-Itoh R. Tertiary lymphoid organs in cancer tissues. Front Immunol 2016;7:244.
[20] Lee SY, Qian CN, Ooi AS, Chen P, Tan VK, Chia CS, et al. Young Surgeon's Award Winner: high endothelial venules: a novel prognostic marker in cancer metastasis and the missing link? Ann Acad Med Singapore2012 2011;41(1):21–8.
[21] Hiraoka N, Ino Y, Yamazaki-Itoh R, Kanai Y, Kosuge T, Shimada K. Intratumoral tertiary lymphoid organ is a favourable prognosticator in patients with pancreatic cancer. Br J Cancer 2015;112(11):1782–90.
[22] Colbeck EJ, Ager A, Gallimore A, Jones GW. Tertiary lymphoid structures in cancer: drivers of antitumor immunity, immunosuppression, or bystander sentinels in disease? Front Immunol 2017;8:1830.
[23] Azzi J, Yin Q, Uehara M, Ohori S, Tang L, Cai K, et al. Targeted delivery of immunomodulators to lymph nodes. Cell Rep 2016;15(6):1202–13.
[24] Bahmani B, Uehara M, Jiang L, Ordikhani F, Banouni N, Ichimura T, et al. Targeted delivery of immune therapeutics to lymph nodes prolongs cardiac allograft survival. J Clin Invest 2018;128:4770–86.
[25] Hiraoka N, Ino Y, Yamazaki-Itoh R, Kanai Y, Kosuge T, Shimada K. Intratumoral tertiary lymphoid organ is a favourable prognosticator in patients with pancreatic cancer. Br J Cancer 2015;112(11):1782–90.
[26] Pandol S, Edderkaoui M, Gukovsky I, Lugea A, Gukovskaya A. Desmoplasia of pancreatic ductal adenocarcinoma. Clin Gastroenterol Hepatol 2009;7(110):S44–7.
[27] Hsiao JR, Leu SF, Huang BM. Apoptotic mechanism of paclitaxel-induced cell death in human head and neck tumor cell lines. J Oral Pathol Med 2009;38(2):188–97.
[28] Ai B, Bie Z, Zhang S, Li A. Paclitaxel targets VEGF-mediated angiogenesis in ovarian cancer treatment. Am J Cancer Res 2016;6(8):1624–35.

[29] Sohal DP, Mangu PB, Khorana AA, Shah MA, Philip PA, O'Reilly EM, et al. Metastatic pancreatic cancer: American Society of Clinical Oncology Clinical Practice Guideline. J Clin Oncol 2016;34(23):2784–96.
[30] Rosenberg A, Mahalingam D. Immunotherapy in pancreatic adenocarcinoma—overcoming barriers to response. J Gastrointest Oncol 2018;9(1):143–59.
[31] Zhang X-W, Ma Y-X, Sun Y, Cao Y-B, Li Q, Xu C-A. Gemcitabine in combination with a second cytotoxic agent in the first-line treatment of locally advanced or metastatic pancreatic cancer: a systematic review and meta-analysis. Target Oncol 2017;12(3):309–21.
[32] Ferrari M. Cancer nanotechnology: opportunities and challenges. Nat Rev Cancer 2005;5:161.
[33] Zhu S, Wonganan P, Lansakara-P DSP, O'Mary HL, Li Y, Cui Z. The effect of the acid-sensitivity of 4-(N)-stearoyl gemcitabine-loaded micelles on drug resistance caused by RRM1 overexpression. Biomaterials 2013;34(9):2327–39.
[34] Fang Y, Du F, Xu Y, Meng H, Huang J, Zhang X, et al. Enhanced cellular uptake and intracellular drug controlled release of VESylated gemcitabine prodrug nanocapsules. Colloids Surf B Biointerfaces 2015;128:357–62.
[35] Bisht S, Mizuma M, Feldmann G, Ottenhof NA, Hong SM, Pramanik D, et al. Systemic administration of polymeric nanoparticle-encapsulated curcumin (NanoCurc) blocks tumor growth and metastases in preclinical models of pancreatic cancer. Mol Cancer Ther 2010;9(8):2255–64.
[36] Bhattacharyya S, Bhattacharya R, Curley S, McNiven MA, Mukherjee P. Nanoconjugation modulates the trafficking and mechanism of antibody induced receptor endocytosis. Proc Natl Acad Sci U S A 2010;107(33):14541–6.
[37] Dancer J, Takei H, Ro JY, Lowery-Nordberg M. Coexpression of EGFR and HER-2 in pancreatic ductal adenocarcinoma: a comparative study using immunohistochemistry correlated with gene amplification by fluorescencent in situ hybridization. Oncol Rep 2007;18(1):151–5.
[38] Patra CR, Bhattacharya R, Wang E, Katarya A, Lau JS, Dutta S, et al. Targeted delivery of gemcitabine to pancreatic adenocarcinoma using cetuximab as a targeting agent. Cancer Res 2008;68(6):1970–8.
[39] Singh A, Xu J, Mattheolabakis G, Amiji M. EGFR-targeted gelatin nanoparticles for systemic administration of gemcitabine in an orthotopic pancreatic cancer model. Nanomedicine 2016;12(3):589–600.
[40] Glazer ES, Zhu C, Massey KL, Thompson CS, Kaluarachchi WD, Hamir AN, et al. Noninvasive radiofrequency field destruction of pancreatic adenocarcinoma xenografts treated with targeted gold nanoparticles. Clin Cancer Res 2010;16(23):5712–21.
[41] Pal K, Al-Suraih F, Gonzalez-Rodriguez R, Dutta SK, Wang E, Kwak HS, et al. Multifaceted peptide assisted one-pot synthesis of gold nanoparticles for plectin-1 targeted gemcitabine delivery in pancreatic cancer. Nanoscale 2017;9(40):15622–34.
[42] Feig C, Gopinathan A, Neesse A, Chan DS, Cook N, Tuveson DA. The pancreas cancer microenvironment. Clin Cancer Res 2012;18(16):4266–76.
[43] Di Maggio F, Arumugam P, Delvecchio FR, Batista S, Lechertier T, Hodivala-Dilke K, et al. Pancreatic stellate cells regulate blood vessel density in the stroma of pancreatic ductal adenocarcinoma. Pancreatology 2016;16(6):995–1004.
[44] Provenzano PP, Cuevas C, Chang AE, Goel VK, Von Hoff DD, Hingorani SR. Enzymatic targeting of the stroma ablates physical barriers to treatment of pancreatic ductal adenocarcinoma. Cancer Cell 2012;21(3):418–29.
[45] Sherman MH, Yu RT, Engle DD, Ding N, Atkins AR, Tiriac H, et al. Vitamin D receptor-mediated stromal reprogramming suppresses pancreatitis and enhances pancreatic cancer therapy. Cell 2014;159(1):80–93.
[46] Chauhan VP, Martin JD, Liu H, Lacorre DA, Jain SR, Kozin SV, et al. Angiotensin inhibition enhances drug delivery and potentiates chemotherapy by decompressing tumour blood vessels. Nat Commun 2013;4:2516.
[47] Desai N, Trieu V, Yao Z, Louie L, Ci S, Yang A, et al. Increased antitumor activity, intratumor paclitaxel concentrations, and endothelial cell transport of cremophor-free, albumin-bound paclitaxel, ABI-007, compared with cremophor-based paclitaxel. Clin Cancer Res 2006;12(4):1317–24.
[48] Liu X, Lin P, Perrett I, Lin J, Liao YP, Chang CH, et al. Tumor-penetrating peptide enhances transcytosis of silicasome-based chemotherapy for pancreatic cancer. J Clin Invest 2017;127(5):2007–18.
[49] Lee SY, Chao-Nan Q, Seng OA, Peiyi C, Bernice WH, Swe MS, et al. Changes in specialized blood vessels in lymph nodes and their role in cancer metastasis. J Transl Med 2012;10:206.
[50] Azzi J, Yin Q, Uehara M, Ohori S, Tang L, Cai K, et al. Targeted delivery of immunomodulators to lymph nodes. Cell Rep 2016;15(6):1202–13.
[51] Kanda M, Fujii T, Nagai S, Kodera Y, Kanzaki A, Sahin TT, et al. Pattern of lymph node metastasis spread in pancreatic cancer. Pancreas 2011;40(6):951–5.
[52] Pelaez-Luna M, Takahashi N, Fletcher JG, Chari ST. Resectability of presymptomatic pancreatic cancer and its relationship to onset of diabetes: a retrospective review of CT scans and fasting glucose values prior to diagnosis. Am J Gastroenterol 2007;102(10):2157–63.
[53] Chen DS, Mellman I. Oncology meets immunology: the cancer-immunity cycle. Immunity 2013;39(1):1–10.
[54] Ueda A, Hosokawa A, Ogawa K, Yoshita H, Ando T, Kajiura S, et al. Treatment outcome of advanced pancreatic cancer patients who are ineligible for a clinical trial. Oncol Targets Ther 2013;6:491–6.
[55] Ager A, May MJ. Understanding high endothelial venules: lessons for cancer immunology. Oncoimmunology 2015;4(6):e1008791.
[56] Martinet L, Garrido I, Filleron T, Le Guellec S, Bellard E, Fournie J-J, et al. human solid tumors contain high endothelial venules: Association with T- and B-lymphocyte infiltration and favorable prognosis in breast cancer. Cancer Res 2011;71(17):5678–87.